J. Fluid Mech. (2014), *vol.* 757, *pp.* 330–353. © Cambridge University Press 2014
doi:10.1017/jfm.2014.469

Fluid migration between confined aquifers

Samuel S. Pegler[1,†], **Herbert E. Huppert**[1,2,3] **and Jerome A. Neufeld**[1,4]

[1]Institute of Theoretical Geophysics, Department of Applied Mathematics and Theoretical Physics, University of Cambridge, Cambridge CB3 0WA, UK

[2]Faculty of Science, University of Bristol, Bristol BS8 1UH, UK

[3]School of Mathematics and Statistics, University of New South Wales, Sydney, NSW 2052, Australia

[4]BP Institute and Department of Earth Sciences, University of Cambridge, Cambridge CB3 0EZ, UK

(Received 25 January 2014; revised 3 June 2014; accepted 8 August 2014;
first published online 19 September 2014)

We study the two-dimensional flow and leakage of buoyant fluid injected at a constant volumetric rate into a fluid-saturated porous medium confined vertically by horizontal boundaries. The upper boundary contains a localized vertical fracture that allows fluid to leak into an open or partially confined porous layer above. The rate of leakage is modelled as proportional to the combined action of the gravitational hydrostatic head of the current below the fracture and the background pressure introduced by the injection. After the injected current reaches the fracture, leakage is initially controlled kinematically by the rate at which injected fluid flows towards the fracture. Once the rate at which buoyant fluid flows towards the fracture exceeds a critical value, the current overshoots the fracture and leakage switches to being controlled dynamically by the pressure drop across the fracture. Two long-term regimes of flow can emerge. In one, the current approaches a steady height above the lower boundary and essentially all fluid injected into the medium leaks at long times. In the other, the current accumulates to fill the entire depth of the medium below the fracture. Only a fraction of the injected fluid then leaks at long times, implying significantly greater long-term storage than has been proposed from studies of leakage from unconfined media. An understanding of the flow regimes is obtained using numerical solutions and analysis of long-term similarity solutions. The implications of our results to the geological storage of carbon dioxide is discussed.

Key words: geophysical and geological flows, gravity currents, porous media

1. Introduction

Fluid flow through porous geological formations is a subject of intense study with wide-reaching applications in both the Earth sciences and industry. Our interest stems primarily from the emerging technology of carbon capture and storage (CCS), in which carbon dioxide (CO_2) is injected into a porous geological formation deep underground (Bickle 2009; Orr 2009; Huppert & Neufeld 2014). As CO_2 is injected into a porous reservoir, it initially rises under buoyancy from the injection well before spreading laterally below a relatively impermeable caprock. Very often, the geological

---

† Email address for correspondence: ssp23@cam.ac.uk

rock contains fractures or permeable faults through which the CO_2 can leak to a higher level in the formation or to the surface. An understanding of leakage is central to the feasibility of CCS.

The theoretical analysis of leakage from porous media has previously focused on cases in which the medium is idealized as infinitely deep (e.g. Pritchard & Hogg 2001; Pritchard 2007; Neufeld, Vella & Huppert 2009; Neufeld *et al.* 2011; Vella *et al.* 2011). In those studies, the fracture was modelled as a distributed sink, with the rate of leakage through it proportional to the hydrostatic head of the current below the fracture. In all such cases, it was found that the current evolves towards a long-term state in which all the fluid injected into the medium leaks, except for an increasing volume of retained fluid flowing downstream of the fracture, which becomes asymptotically small relative to the total volume injected. In a two-dimensional aquifer, for example, the ratio of fluid retained to fluid injected, defined as an efficiency of storage, decays as $t^{-1/2}$, implying that the rate of leakage approaches the rate of injection (Neufeld *et al.* 2009). By assuming that the aquifer is infinitely deep, these earlier studies precluded any dynamical controls on leakage introduced by vertical confinement.

Seismic measurements at CCS test sites have indicated that the CO_2 currents produced have comparable thickness to the depth of the aquifer (e.g. Boait *et al.* 2012). Particularly when the injected fluid is much less viscous than the ambient fluid, as is relevant to CCS, vertical confinement introduces new effects that do not occur when the medium is idealized as unconfined (Nordbotten & Celia 2006; Pegler, Huppert & Neufeld 2014). One is the build-up of an additional, non-gravitational background pressure associated with the pressurization at the injection. We show how this added pressure contributes to driving leakage through fractures. Similar contributions have been included in reduced models of fluid leakage between stacked reservoirs (Nordbotten *et al.* 2005, 2009), but these models neglect the detailed interactions between the current and its leakage. Here, we develop and solve general model equations that describe this interaction and thus elucidate the important fluid-mechanical balances and flow regimes that emerge.

The second effect introduced by confinement is to limit the maximum possible accumulation of the injected current below the fracture. This contrasts with unconfined aquifers, where the current can accumulate without limit. Importantly, this constraint is shown to limit the contribution to leakage due to gravity and result in a maximum possible rate of leakage. Consequently, one of two possible long-term flow regimes can emerge, dependent on whether the rate of injection exceeds the maximum rate of leakage. With these new dynamical considerations included, we show that the long-term storage efficiency can be orders of magnitude greater than has been proposed previously from studies of unconfined media with otherwise identical flow parameters.

We begin in § 2 by developing our theoretical model describing a current of buoyant fluid injected into a fractured porous layer. In § 3, we identify the differing dynamical regimes described by the model. In § 4, we consider the predictions of the model in an illustrative geophysical setting before summarizing our conclusions in § 5.

2. Theoretical development

Consider a viscous fluid of dynamic viscosity μ and density ρ injected at the constant volumetric rate per unit width Q_0 into a two-dimensional porous medium of uniform permeability k and porosity ϕ saturated by an ambient fluid of dynamic

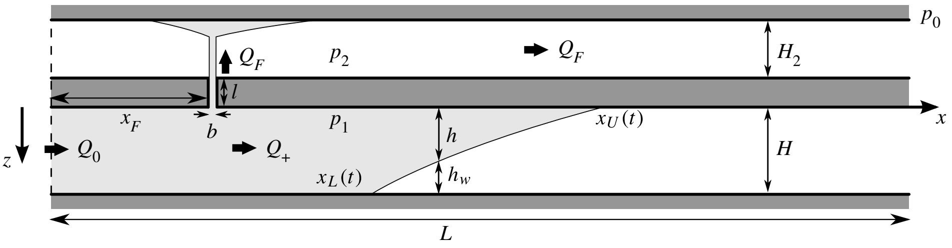

FIGURE 1. Cross-section of a two-dimensional porous medium containing horizontal boundaries along $z=-(l+H_2)$, $-l$, 0 and H, forming two parallel porous layers or 'aquifers'. A vertical outlet, the 'fracture', centred on $x=x_F$, provides a conduit between the lower and upper layers. The buoyant fluid injected into the lower layer is shown shaded and its sharp interface $z=h(x,t)$ is shown as a thin curve.

viscosity μ_a and larger density $\rho_a>\rho$ (see figure 1). The medium comprises two porous layers, or 'aquifers', formed from four impermeable horizontal boundaries along $z=-(l+H_2)$, $-l$, 0 and H. This configuration is motivated by the layered formations characteristic of many geological reservoirs (Nordbotten *et al.* 2005; Boait *et al.* 2012). Leakage to effectively unconfined regions, such as the atmosphere or ocean, is accommodated within our model by letting $H_2\gg H$. The two fluids in the lower layer are assumed to be separated at all times by a sharp interface $z=h(x,t)$ (Bear 1988), which generally intersects the upper and lower boundaries along two contact lines $x=x_U(t)$ and $x=x_L(t)$, respectively. A narrow gap, the 'fracture', of horizontal breadth b and vertical length l, is centred on $x=x_F$ and provides a conduit between the layers. With respect to a constant reference pressure $p_0\equiv p(L,-(H_2+l),t)$ at a location $x=L$ along the top of the upper layer, the fluid pressure $p=p(x,z,t)$ is specified on $x=L$ as

$$p(L,z,t)=p_0+\rho_a g(z+H_2+l). \tag{2.1}$$

In the geological context, the position $x=L$ could be interpreted as the terminus of an interstitial impermeable boundary or an opening or fault connecting the aquifer to another reservoir, the atmosphere or the ocean.

Assuming that the horizontal length scales of the flow are much larger than the thickness of the current ($x_F, x_L, x_U\gg h$), we model the evolution of the interface in the lower layer using the nonlinear diffusion developed by Pegler *et al.* (2014) as

$$\phi\frac{\partial h}{\partial t}+\frac{\partial q}{\partial x}=0, \quad \text{where} \quad q\equiv\frac{h\left\{\lambda Q(x,t)-\lambda_a U(H-h)\dfrac{\partial h}{\partial x}\right\}}{\lambda h+\lambda_a(H-h)} \tag{2.2a,b}$$

is the volumetric flux of the current per unit width and

$$Q(x,t)=\begin{cases} Q_0 & \text{if } x<x_F, \\ Q_+(t)\equiv Q_0-Q_F(t) & \text{if } x>x_F, \end{cases} \tag{2.3}$$

is the total flux per unit width of both the current and the ambient fluid in the lower layer, respectively. The quantity $U\equiv\lambda\Delta\rho g$ is the buoyancy speed, $\Delta\rho\equiv\rho_a-\rho$ is the density difference, $\lambda\equiv k/\mu$ is the mobility of the buoyant fluid and $\lambda_a\equiv k/\mu_a$ is the mobility of the ambient fluid. Without leakage, the total flux $Q \equiv Q_0$ everywhere and the equations reduce to those considered by Pegler *et al.* (2014). With leakage, the total flux instead divides at $x = x_F$ between the leaked flux Q_F and the retained flux $Q_+(t) \equiv Q_0 - Q_F(t)$. We refer to $Q_F(t) \equiv q_F(t) + q_A(t)$ as the 'total' leakage flux, which generally contains contributions due to both the current $q_F(t)$ and the ambient fluid $q_A(t)$.

When the interface lies between the boundaries of the medium at the injection ($h(0, t) < H$), the combination of $q(0, t) = Q_0$ and (2.2b) yields the boundary condition

$$-Uh\frac{\partial h}{\partial x} = Q_0 \quad \text{at } x = 0 \text{ if } h(0, t) < H \tag{2.4}$$

(Pegler *et al.* 2014). Following that study, we also impose the contact-line conditions

$$h = 0, \quad \phi \dot{x}_U = \frac{Q}{MH} - U\frac{\partial h}{\partial x} \quad \text{at} \quad x = x_U, \tag{2.5a,b}$$

$$h = H, \quad \phi \dot{x}_L = \frac{MQ}{H} + MU\frac{\partial h}{\partial x} \quad \text{at } x = x_L \text{ if } h(0, t) = H, \tag{2.6a,b}$$

where $M \equiv \lambda_a/\lambda = \mu/\mu_a$ is the mobility ratio. Conditions (2.5) and (2.6) follow from the continuity of the interface and flux of each fluid layer (Pegler *et al.* 2014). We apply (2.4) before the current spans the depth of the medium at $x = 0$ and (2.6*a*,*b*) afterwards.

If the horizontal extent of the region of leakage b is small ($b \ll H, x_U$), then we can impose the leading-order continuity conditions across it given by

$$h_- = h_+, \quad q_+ - q_- = Q_F \quad \text{at } x = x_F, \tag{2.7a,b}$$

where the ± subscripts denote quantities downstream or upstream of the fracture, respectively. Condition (2.7*a*) follows from a horizontal balance of depth-integrated hydrostatic pressure between regions either side of the fracture. Conditions (2.7*a*,*b*) differ from the distributed sink applied by Pritchard & Hogg (2001) and Neufeld *et al.* (2009) but become asymptotically equivalent in the limit of small breadth b.

We model the leakage using Darcy's law (Bear 1988),

$$Q_F = \frac{b\lambda_F}{l}(p_1 - p_2 - \rho g l) \quad \text{at } x = x_F, \tag{2.8}$$

where $\lambda_F \equiv k_F/\mu$ is the mobility of the injected fluid in the fracture and k_F is the permeability of the fracture, while $p_1 \equiv p(x, 0, t)$ and $p_2 \equiv p(x, -l, t)$ are the fluid pressures at the base and top of the fracture, respectively. An allowance for the leakage of ambient fluid will be discussed later in this section. For a thin layer, the stresses due to vertical flow are negligible and pressure is purely hydrostatic (Bear 1988). Consistent with the reference pressure (2.1), the hydrostatic pressure distributions along the top boundary of the lower layer and along the bottom boundary of the upper layer are given as

$$p_1(x, t) \equiv p(x, 0, t) = P_1(x, t) + p_0 + \rho_a g(H_2 + l) + \Delta\rho g h, \tag{2.9}$$

$$p_2(x, t) \equiv p(x, -l, t) = P_2(x, t) + p_0 + \rho_a g H_2, \tag{2.10}$$

respectively, where $P_1(x, t)$ and $P_2(x, t)$ are the unknown background pressure distributions, or non-gravitational contributions to pressure, arising from confined horizontal flow (Pegler *et al.* 2014). Note that, while p_1 depends on the hydrostatic head h in the lower layer, there is no analogous dependence of p_2 on the accumulation of fluid in the upper layer because a gravity current only perturbs hydrostatic pressure in its interior. Using (2.9) and (2.10) to evaluate p_1 and p_2 in (2.8), we obtain

$$Q_F = \frac{b\lambda_F}{l}[P_1 - P_2 + \Delta\rho g(h+l)] \quad \text{at } x = x_F. \tag{2.11}$$

Importantly, (2.11) implies that leakage is driven both by the difference in background pressure $(P_1 - P_2)$ between the two layers and by the hydrostatic head of the buoyant current below the fracture. The former is a new contribution to leakage compared to unconfined aquifers, where only the latter contributes to driving leakage.

By combining Darcy's law with the constraint on the total thickness of the flow, the background pressure along the lower layer P_1 can be shown to satisfy

$$-[\lambda h + \lambda_a(H-h)]\frac{\partial P_1}{\partial x} + \Delta\rho g\lambda_a(H-h)\frac{\partial h}{\partial x} = Q(t) \tag{2.12}$$

(Pegler *et al.* 2014). A similar expression could be written down for the background pressure P_2 in the upper layer. Rearranging (2.12) for $\partial P_1/\partial x$ and then integrating over $[x_F, L]$ subject to the specified downstream background pressure $P_1(L,t) = 0$ consistent with (2.1), we determine the 'back-pressure' below the fracture as

$$\begin{aligned} P_1(x_F,t) \;=\; & \frac{(x_L - x_F)}{\lambda H}Q_+ + \frac{(L - x_U)}{\lambda_a H}Q_+ \\ & + \int_{x_L}^{x_U} \frac{Q_+ - \Delta\rho g\lambda_a(H-h)\dfrac{\partial h}{\partial x}}{\lambda h + \lambda_a(H-h)}\,\mathrm{d}x. \end{aligned} \tag{2.13}$$

The respective terms in (2.13) represent the background pressure driving fluid between: the fracture and the lower contact line ($x_F < x < x_L$); the current and the end of the aquifer ($x_U < x < L$); and the fluid fronts ($x_L < x < x_U$). Note that (2.13) is applicable in situations where the current spans the depth of the medium below the fracture ($h(x_F,t) = H$). If, instead, the interface lies between the fracture and the lower boundary ($h(x_F,t) < H$), then an expression similar to (2.13) applies but with the first term absent and x_F replacing x_L in the lower limit of the integral.

We simplify (2.13) in situations motivated by CCS as follows. If the aquifer is long compared to the current, then the contribution to the back-pressure (2.13) due to ambient displacement $LQ_+/\lambda_a H$ is significantly larger than the other contributions. More formally, this contribution and its analogue in the upper layer are dominant if $L \gg Mx_U$, for which

$$P_1(x_F,t) \approx \frac{LQ_+}{\lambda_a H}, \quad P_2(x_F,t) \approx \frac{LQ_F}{\lambda_a H_2}. \tag{2.14a,b}$$

In other words, the background pressures at the bottom and top of the fracture, P_1 and P_2, can each be approximated as originating from the pressure build-up associated with driving ambient fluid along the lower and upper layers, respectively.

Using (2.14*a,b*) to evaluate P_1 and P_2 in (2.11), we obtain

$$\frac{lQ_F}{b\lambda_F} = \frac{LQ_+}{H\lambda_a} - \frac{LQ_F}{H_2\lambda_a} + \Delta\rho g(h+l). \tag{2.15}$$

The first term on the right-hand side represents leakage driven by the pressure build-up arising from the displacement of ambient fluid along the lower layer. The second represents the resistance to leakage due to the viscous stresses associated with mobilizing ambient fluid along the upper layer. The last term represents leakage driven by the combination of the hydrostatic head and gravity along the fracture. Using (2.3) to substitute for Q_+ in favour of Q_F in (2.15), we obtain

$$(1+\varGamma+\varGamma_F)Q_F = Q_0 + \frac{\Delta\rho g \lambda_a H^2}{L}\left[\frac{h(x_F,t)}{H}+\delta\right], \tag{2.16}$$

where

$$\varGamma \equiv \frac{H}{H_2}, \quad \varGamma_F \equiv \frac{lH_2\lambda_a}{bL\lambda_F} \quad \text{and} \quad \delta \equiv \frac{l}{H}. \tag{2.17a–c}$$

The ratio of aquifer thicknesses $\varGamma$ measures the relative resistance to displacing ambient fluid along the lower layer compared to the upper layer. At Sleipner, for example, the sandstone layers have comparable thicknesses (Boait *et al.* 2012) and hence $\varGamma = O(1)$. In situations where the fracture connects the aquifer to the atmosphere or ocean, $H_2 \gg H$ and $\varGamma \approx 0$. The parameter δ is the ratio of the length of the aquifer to the thickness of the lower layer and measures the relative contribution to the leakage rate due to gravity acting along the fracture compared to the maximum that can be driven by the hydrostatic head below it. The depths of sandstone layers $H = O(10\ \text{m})$ are generally greater than those of the interstitial layers $l = O(1\ \text{m})$ at Sleipner, for which $\delta = O(10^{-1})$. The parameter $\varGamma_F$ measures the relative resistance to leakage due to the back-pressure associated with mobilizing ambient fluid along the upper layer compared to the back-pressure generated by viscous stresses acting inside the fracture itself. To estimate an upper bound for $\varGamma_F$, we use the characteristically small fracture aperture $b = O(10^{-4}\ \text{m})$ (Singhal & Gupta 2010). Treating the flow as a Poiseuille flow, we estimate the permeability of the fracture as $k_F = b^2/12 \approx O(10^{-9}\ \text{m}^2)$. Combining this with the typical viscosity ratio $M = \mu/\mu_a \approx 0.1$, aquifer length $L = O(10\ \text{km})$ and permeability $k = 10^{-12}\ \text{m}^2$ (Boait *et al.* 2012), we obtain $\varGamma_F = O(10^{-3})$. Larger apertures b and aquifer lengths L would imply yet smaller values of $\varGamma_F$. Prior studies of unconfined aquifers have assumed that the resistance to leakage stems purely from the viscous stresses within the fracture. Our estimate of $\varGamma_F$ indicates that the back-pressure due to displacing ambient fluid along the upper layer introduces a dynamic resistance to leakage that has the potential to be many orders of magnitude more significant.

In obtaining (2.16), we supposed that the fluid leaking through the fracture is composed purely of injected fluid. As we detail later, it is possible for either purely ambient fluid or a combination of both injected and ambient fluids to leak simultaneously. When only ambient fluid leaks, for example, the relevant mobility λ_F appearing in (2.15) should be replaced by $M^{-1}\lambda_F$. Apart from the special case $M = 1$, $\varGamma_F$ is dependent on the relative contributions to leakage due to the ambient and injected fluids, so $\varGamma_F = \varGamma_F(q_F/Q_F)$. Here, we avoid a detailed consideration of the effective fracture mobility when combined leakage occurs by neglecting $\varGamma_F$ in (2.16). The lower-bound order-of-magnitude estimate of $\varGamma_F = O(10^{-3})$ indicates that these neglected details do not play a significant role.

Another change to (2.16) that would apply when purely ambient fluid leaks is to remove any contribution to leakage due to buoyant fluid in the fracture, represented by δ. A model that accounts for this contribution could be achieved by replacing δ with the linear function $\delta q_F/Q_F$, for example. However, in view of the small estimate of δ given above and to simplify our discussion of the transient leakage of ambient fluid, we neglect this dependence ($\delta \ll 1$). Were it instead retained, its effect on the long-term predictions of our model can be straightforwardly incorporated by absorbing δ into the constant Q_B appearing in the simplified leakage law (2.18) below.

With the simplifications described above ($\varGamma_F, \delta \approx 0$), (2.16) reduces to

$$Q_F = Q_B + Q_G h(x_F, t)/H, \tag{2.18}$$

where

$$Q_B \equiv \frac{Q_0}{1+\varGamma} \quad \text{and} \quad Q_G \equiv \frac{\Delta\rho g \lambda_a H^2}{(1+\varGamma)L}. \tag{2.19a,b}$$

The constant Q_B represents leakage driven by the back-pressure. It is a lower bound for the total rate of leakage ($Q_F \geqslant Q_B$). The quantity Q_G defined by (2.19*b*) represents the contribution to leakage due to the largest gravitational pressure head that can fit below the fracture (occurring when $h(x_F, t) = H$). As implied by (2.18), the rate of leakage due to gravity is generally given by the product of Q_G and $h(x_F, t)/H$, the proportion of the layer immediately below the fracture filled by the current. Given that $0 < h < H$, (2.18) implies that Q_F always lies in the range

$$Q_B \leqslant Q_F \leqslant Q_B + Q_G \ (\equiv Q_{max}). \tag{2.20}$$

The inequalities in (2.20) illustrate how confinement introduces two opposing effects. In the first, background pressure enhances leakage by contributing to the lower bound Q_B. In the second, the constraint on the hydrostatic head ($h \leqslant H$) restricts leakage by implying a maximum possible rate of leakage Q_{max}. The relative significance between these two effects in the geological context will be considered in § 4.

The leakage law (2.18) describes the total leakage rate $Q_F = q_F + q_A$, to which both the injected and ambient fluids can contribute. We determine their individual contributions by imposing

$$q_F = \begin{cases} q_- & \text{if } q_- < Q_F \ \text{(kinematic leakage)}, \\ Q_F & \text{if } q_- > Q_F \ \text{(dynamic leakage)}. \end{cases} \tag{2.21}$$

Condition (2.21) states that if $q_- < Q_F$ then all the injected fluid reaching the fracture leaks through it. This follows from the fact that accumulation of the current cannot occur before the rate at which buoyant fluid reaches the fracture exceeds the rate at which it leaks. Once $q_- > Q_F$, (2.21) states that only injected fluid leaks ($q_A = 0$). This is consistent with the requirement that, once $q_+ = q_- - Q_F > 0$, the current overshoots the fracture to form a barrier that precludes any ambient fluid from leaking. In summary, the total rate of leakage Q_F is always controlled dynamically by the leakage law (2.18). However, the leakage of the injected fluid q_F can be controlled either kinematically by the rate at which the current flows towards the fracture or dynamically by the balances underlying (2.18).

3. Theoretical analysis

Equations (2.2)–(2.7) and (2.18) can be non-dimensionalized by defining

$$(x, x_U, x_L) \equiv \mathscr{L}(\hat{x}, X_U, X_L), \quad t \equiv \mathscr{T}\hat{t}, \quad h \equiv H\hat{h}, \quad (q, Q) \equiv Q_0(\hat{q}, \widehat{Q}), \tag{3.1a–d}$$

where

$$\mathscr{L} \equiv UH^2/Q_0 \quad \text{and} \quad \mathscr{T} \equiv \phi UH^3/Q_0^2 \tag{3.2a,b}$$

are the same intrinsic scales for two-dimensional flows in confined porous media as obtained by Pegler *et al.* (2014). On dropping hats, (2.2) and (2.3) become

$$\frac{\partial h}{\partial t}+\frac{\partial}{\partial x}\left[\frac{h\left\{Q(x,t)-M(1-h)\dfrac{\partial h}{\partial x}\right\}}{h+M(1-h)}\right]=0, \tag{3.3}$$

$$Q(x,t)=\begin{cases}1 & \text{if } x<X_F,\\ 1-Q_F(t) & \text{if } x>X_F.\end{cases} \tag{3.4}$$

The source condition (2.4) becomes

$$-h\frac{\partial h}{\partial x}=1 \quad \text{at } x=0 \text{ if } h(0,t)<1, \tag{3.5}$$

and the contact-line conditions (2.5) and (2.6) become

$$h=0, \quad \dot{X}_U=M^{-1}Q-\frac{\partial h}{\partial x} \quad \text{at } x=X_U, \tag{3.6a,b}$$

$$h=1, \quad \dot{X}_L=MQ+M\frac{\partial h}{\partial x} \quad \text{at } x=X_L \text{ if } h(0,t)=1. \tag{3.7a,b}$$

The continuity conditions (2.7*a*,*b*) become

$$h_-=h_+, \quad -h_-\left[\frac{\partial h_-}{\partial x}-\frac{\partial h_+}{\partial x}\right]=Q_F \quad \text{at } x=X_F. \tag{3.8a,b}$$

The leakage law (2.15) becomes

$$Q_F(t)=B+D^{-1}(1-B)\,h \quad \text{at } x=X_F, \tag{3.9}$$

and the condition describing the rate of leakage of the current (2.21) becomes

$$q_F=\begin{cases}q_- & \text{if } q_-<Q_F,\\ Q_F & \text{if } q_->Q_F.\end{cases} \tag{3.10}$$

The non-dimensionalized system depends on four dimensionless parameters

$$M\equiv\frac{\lambda_a}{\lambda}, \quad B\equiv\frac{1}{1+\varGamma}, \quad D\equiv\frac{\varGamma ML}{\mathscr{L}}, \quad X_F\equiv\frac{x_F}{\mathscr{L}}, \tag{3.11a–d}$$

representing the mobility ratio, the dimensionless rate of leakage due to the injection pressure, the dimensionless hydrostatic head of the current at which the injection rate equals the leakage rate (see (3.15) below), and the dimensionless fracture position.

The dimensionless form of the inequality (2.20) is

$$B<Q_F<Q_{max}\equiv B+D^{-1}(1-B). \tag{3.12}$$

The parameter B is the dimensionless form of the minimum rate of total leakage. Equation (3.11*b*) implies that $0\leqslant B\leqslant 1$ and hence that the leakage driven purely by

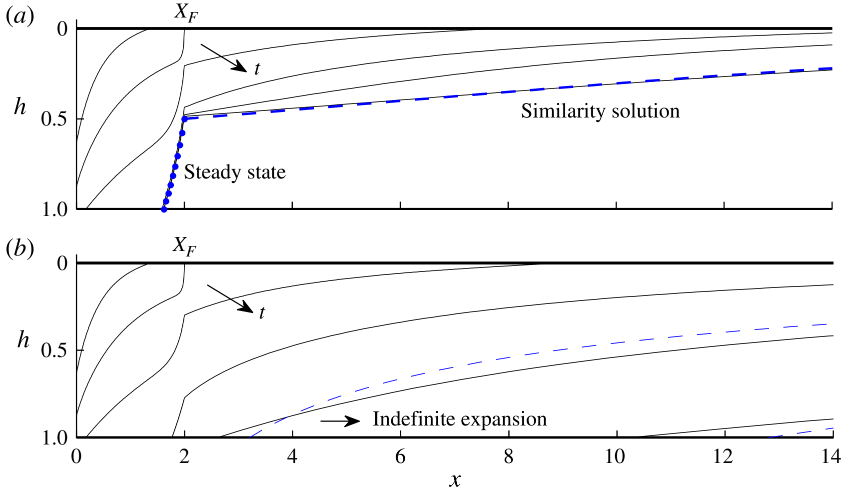

FIGURE 2. (Colour online) The evolution of the interface height $h(x, t)$ for hydrostatic parameters (*a*) $D = 0.5$ and (*b*) $D = 2$, each with $B = 0.5$, $M = 0.2$ and $X_F = 2$ plotted at times $t = 0.25$, 1, 4, 16, 64 and 256. The plots illustrate the markedly different long-term flow regimes that arise between cases of (*a*) $D \leqslant 1$ and (*b*) $D > 1$. In (*a*), the region upstream of the fracture approaches the steady profile (3.17*b*) (dotted) and the flow downstream approaches the time-dependent similarity solution of (3.20)–(3.22) (thick, dashed). In (*b*), the current spans the depth of the medium below the fracture and approaches the long-term similarity solution (3.32*a*) (thin, dashed).

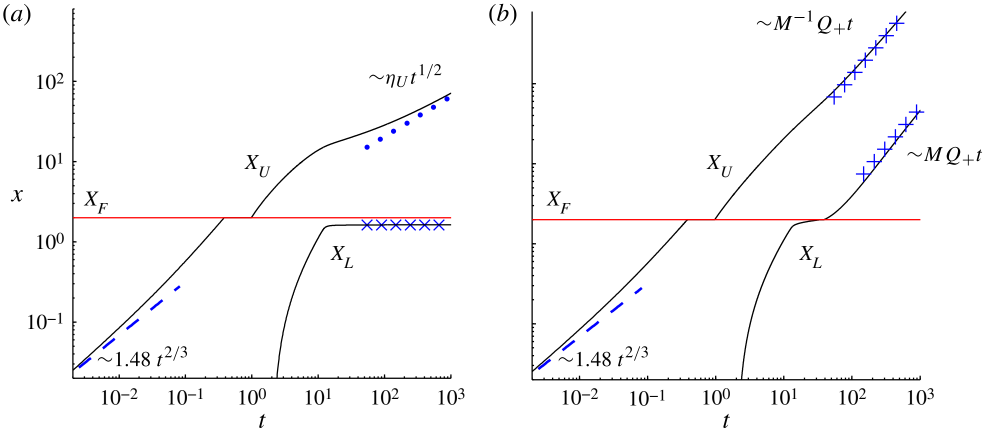

FIGURE 3. (Colour online) The evolution of the upper and lower contact lines $X_U(t)$ and $X_L(t)$ for (*a*) $D = 0.5$ and (*b*) $D = 2$, each with $B = 0.5$, $M = 0.2$ and $X_F = 2$. The position of the fracture X_F is indicated by a horizontal grey (red online) line. The early-time asymptote $X_U \sim 1.48\, t^{2/3}$ is shown as a dashed line in each panel. The long-term frontal position (3.30*b*) that applies when $D \leqslant 1$ is shown as a line of dots in (*a*). The long-term steady-state position of the lower contact line implied by (3.17*b*) is shown as a line of crosses. The long-term asymptotic positions of the two contact lines (3.32*b*,*c*) when $D > 1$ are shown as lines of plus signs in (*b*).

the back-pressure cannot exceed the injection rate. The special case $B=0$ describes situations where leakage depends only on accumulation ($Q_F = h(x_F, t)/D$). The case $B=1$ corresponds to situations when all fluid flowing towards the fracture leaks through it ($Q_F=1$), in accord with (3.9). This scenario would arise in physical settings where there is a direct opening to the atmosphere or ocean that affords effectively no resistance to leakage ($\varGamma \approx 0$). The hydrostatic parameter D appearing in (3.9) controls the rate of leakage due to gravity. Smaller D implies greater gravity-driven leakage for a given hydrostatic head $h(x_F, t)$. The limit $D \to \infty$ describes situations where the leakage is driven purely by the injection pressure ($Q_F = B$). Cases of $M \ll 1$ describe situations where the injected fluid is much less viscous than the ambient fluid, as is relevant to CCS. The joint limit $D, X_F \to 0$ implies a thin current relative to the medium ($h \to 0$) for which the model reduces asymptotically to that which describes flow in an unconfined medium (Neufeld *et al.* 2009). As we detail in § 4, $M=O(10^{-1})$, $B=O(1)$, $D=O(10)$ and $X_F=O(1)$ are estimates motivated by sequestration at Sleipner.

3.1. *The transient flow*

Two illustrative numerical solutions of (3.3)–(3.10) are shown in figure 2(*a*,*b*). Here, we have plotted the interface $h(x, t)$ at times $t=0.25,\ 1,\ 4,\ 16,\ 64$ and 256 for $D=0.5$ and 2, respectively, both with $B=0.5$, $M=0.2$ and $X_F=2$. The solutions were obtained using a partially implicit two-step finite-difference scheme of second order and variable time step in which the time-dependent numerical domains of the current upstream $[0, \max(x_U, x_F)]$ and downstream $[x_F, x_N]$ were each mapped linearly onto fixed domains. Steep gradients in the interface h immediately upstream of the fracture (see figure 4*b* and (3.13) below) present a numerical difficulty in the evaluation of the flux of the current towards the fracture q_- needed in (3.8*b*) and (3.10). Noting that q remains regular, despite the steep gradients in h, we addressed this difficulty by approximating q_- as a linear extrapolation of q towards the fracture.

The solutions illustrate two different flow regimes. When $D=0.5$, the flow upstream of the fracture approaches a steady state (see figure 2*a*). At all times, the interface below the fracture remains in the interior of the medium ($h(X_F, t) < 1$) and the lower contact line converges towards a steady position $X_L(t) \to 1.625 < X_F$. As this convergence occurs, the flow downstream of the fracture continues to propagate time-dependently. When $D=2$, the current instead grows to fill the entire depth of the medium below the fracture, with $h(X_F, t)=1$ occurring at $t \approx 35$ (see figure 2*b*). At that time, the lower contact line overshoots the fracture. It then continues to propagate downstream indefinitely ($X_L(t) \to \infty$), as illustrated in figure 3(b).

In the initial stages, before the current reaches the fracture ($X_U < X_F$), the evolution is equivalent to that of a current injected into a medium with no fracture (Pegler *et al.* 2014). In that analysis, we showed that the early-time propagation in all such examples is described by $X_U \sim 1.48 t^{2/3}$, the self-similar propagation that also describes a current fed at a constant flux into an unconfined two-dimensional medium (Huppert & Woods 1995). This asymptote, shown by the dashed lines in figure 3(*a*,*b*), matches our numerical solutions at early times.

In figure 4(*a*–*c*), we have illustrated three transitional stages that occur as the current first interacts with the fracture. Before the current reaches the fracture (figure 4*a*), only ambient fluid leaks, $q_A = Q_F = B$, in accord with (3.9) and (3.10). This initial equivalence is illustrated in figure 4(*d*), where the evolution $Q_F(t)$ is plotted as the red curve, and the injected and ambient contributions to Q_F, denoted

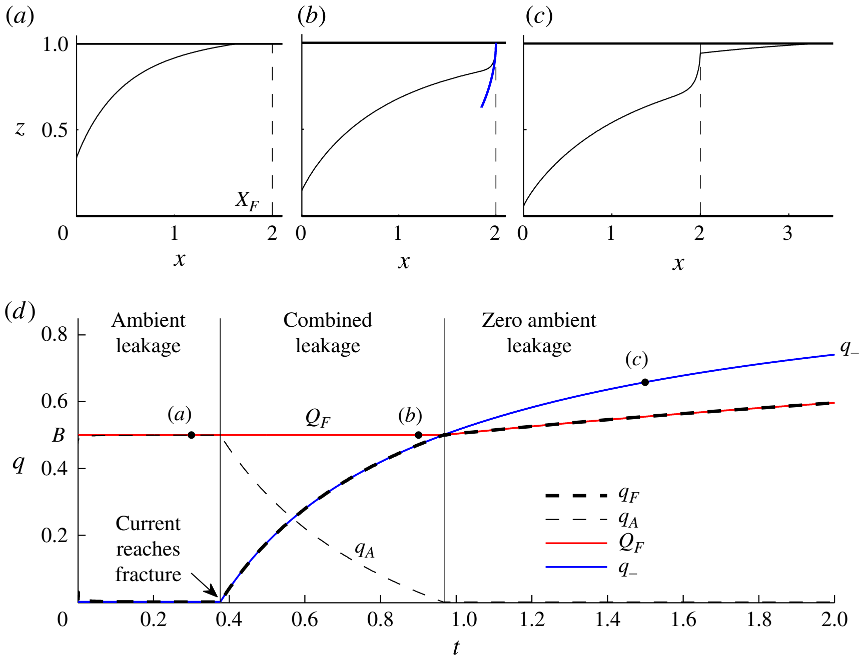

FIGURE 4. The interface height $h(x, t)$ at times (*a*) $t = 0.3$, (*b*) $t = 0.9$ and (*c*) $t = 1.5$ for $B = 0.5$, $D = 0.5$, $M = 0.2$ and $X_F = 2$. The sequence has three stages: (*a*) the current lies entirely upstream of the fracture; (*b*) the front remains temporarily pinned at the fracture; and (*c*) the current overshoots the fracture. The asymptote (3.13) is shown as a blue curve in (*b*). (*d*) The leakage rate of injected fluid q_F (thick, dashed), ambient fluid q_A (thin, dashed), the total leakage of both fluids $Q_F = q_F + q_A$ (red, solid) and the flux of the current towards it q_- (blue, solid), as functions of time t. The plot shows the transition from purely ambient leakage for $t \lesssim 0.38$, to combined leakage for $0.38 \lesssim t \lesssim 0.97$ and to zero ambient leakage for $t \gtrsim 0.97$. Propagation downstream of the fracture ($q_+ = q_- - Q_F > 0$) occurs once $q_- > B$. Subsequent enhancement of the total leakage flux Q_F occurs due to growth of the hydrostatic head below the fracture.

by $q_F(t)$ and $q_A(t)$, are shown by the thicker and thinner dashed black curves, respectively.

Once the current reaches the fracture at $t \approx 0.38$, the flux of the current towards it, q_-, shown by the blue curve, begins to increase from zero. Initially, the total rate of leakage Q_F exceeds the rate at which the current flows towards the fracture ($q_- < Q_F$). The leakage of injected fluid is therefore initially controlled kinematically in accord with (2.21*b*). The equivalence $q_F = q_-$ is illustrated in figure 4(*d*). During this transient stage, shown in figure 4(*b*), the front of the current remains temporarily pinned at the fracture with a vanishing thickness ($h(X_F, t) = 0$) but a finite flux ($q_-(t) > 0$). By considering the form of the flux of the current (2.2*b*) in the asymptotic limit $h \to 0$ with $q = q_-$ held finite, we obtain the leading shape of the current

$$h \sim [2q_-(t)(X_F - x)]^{1/2} \quad (x \to X_F^-). \tag{3.13}$$

This asymptote, which describes a singular gradient at the fracture, is shown by the blue curve in figure 4(b).

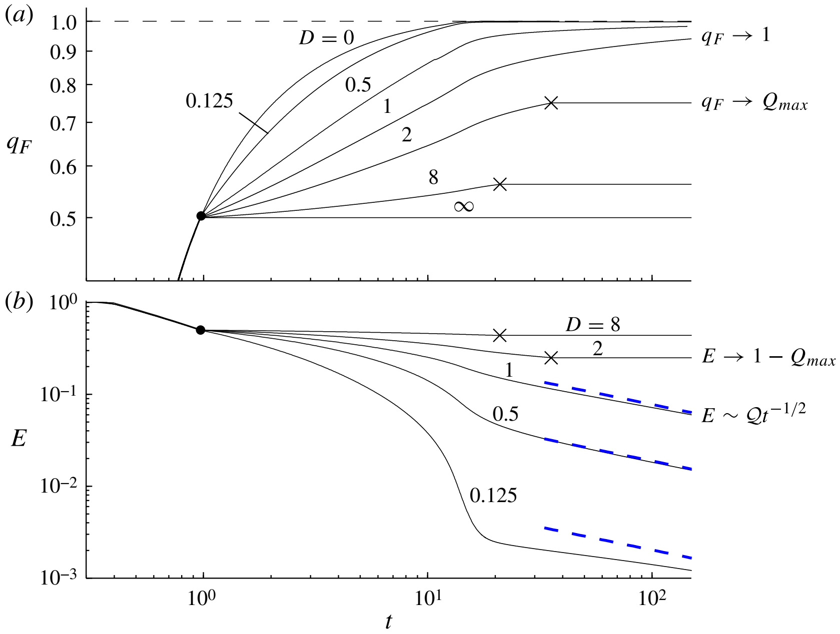

FIGURE 5. (Colour online) (a) The evolution of the rate of leakage of the current q_F for a selection of hydrostatic parameters $D = 0$, 0.125, 0.5, 1, 2 and 8, all with the illustrative background leakage parameter $B = 0.5$. When $D \leqslant 1$, the rate asymptotes towards the injection flux ($q_F \sim 1$), shown by a horizontal dashed line. When $D > 1$, q_F attains the value (3.33b) less than unity. The time at which the current overshoots the fracture is shown as a filled circle. Times when the current accumulates to fill the depth of the medium below the fracture are shown as crosses for $D = 2$ and 8. (b) The efficiency of storage $E(t)$, defined by (3.14), showing its approach towards the asymptote (3.19c) if $D \leqslant 1$ and (3.31) if $D > 1$.

At $t \approx 0.97$, the flux of the current towards the fracture first exceeds the total leakage rate ($q_- > Q_F$), causing the leakage of injected fluid q_F to switch to being controlled dynamically by the total leakage rate (3.10b). The residual $q_+ = q_- - q_F$ then begins to feed flow downstream of the fracture ($X_U > X_F$), as illustrated in figure 4(c).

With $D = 0.5$, the position of the interface below the fracture approaches the long-term asymptotic height $h \sim 0.5$ in the vertical interior of the medium. The plot in figure 3(a) indicates that the position of the upper contact line is $X_U = O(t^{1/2})$ for $t \to \infty$. Furthermore, figure 5(a) indicates that the rate of leakage of the current q_F converges towards the rate of injection ($q_F \sim 1$). Therefore, almost all fluid injected into the medium leaks in the long term. The efficiency of storage, defined as

$$E(t) \equiv 1 - q_F(t) \tag{3.14}$$

(cf. Neufeld *et al.* 2011), provides an instantaneous measure of the rate at which buoyant fluid is retained in the lower layer normalized by its rate of injection. The plot of $E(t)$ in figure 5(b) shows that $E = 1$ before the current reaches the fracture, consistent with no leakage. Once leakage begins, E decreases. At late times, $E \to 0$. Apart from a minor residual, almost all of the fluid injected into the medium therefore leaks. This mode of decay is qualitatively identical to that determined by Neufeld *et al.* (2009) in the context of unconfined aquifers. Figure 5(*b*) shows that E similarly decays for other values of $D \leqslant 1$. The asymptotes describing this decay will form the focus of § 3.2.

When $D = 2$, the current fills the entire depth of the medium below the fracture. Instead of approaching a steady position, as it does for $D \leqslant 1$, the lower contact line X_L extends ahead of the fracture ($X_L > X_F$) and continues to propagate forwards indefinitely. Figure 3(*b*) indicates that both contact lines eventually grow in proportion with time (X_U, $X_L = O(t)$) but with differing constants of proportionality. When the current fills the depth of the aquifer ($h(X_F, t) = 1$), the leakage rate of the current q_F attains the maximum $q_F = Q_{max} < 1$ in (3.12). The times at which this occurs are shown as crosses in figure 5(*a*,*b*). Importantly, the efficiency of storage $E \rightarrow 1 - Q_{max}$ does not decay. This differs from the conclusions drawn from studies of unconfined aquifers, and the case $D = 0.5$ described above, and implies the potential for substantially greater long-term storage in confined aquifers.

In summary, the solutions with $D = 0.5$ and $D = 2$ illustrate two regimes of flow distinguished by whether the interface approaches a steady position in the vertical interior of the medium or accumulates to fill its full depth. We determine the parameter settings under which the former regime arises by considering the conditions for which convergence towards a steady interface upstream of the fracture can occur. With steady flow ($\partial h/\partial t = 0$), the continuity equation (2.2*a*) implies that $q = 1$ is uniform in $0 < x < X_F$. For this steady state to be realized, the leakage rate (2.18) must balance the injection rate, so

$$q = Q_F = B + D^{-1}(1 - B)\, h \sim 1 \quad \text{or} \quad h \sim D. \tag{3.15a,b}$$

From (3.15*b*), we see that D can be interpreted as the long-term steady thickness of the current below the fracture. In order for the asymptotic approach of (3.15*a*,*b*) to be possible, it is necessary that $D \leqslant 1$. Otherwise, the interface would penetrate the lower boundary ($h > 1$). An equivalent interpretation is that $D \leqslant 1$ corresponds to when the leakage flux can grow to match the injection flux. This is confirmed by noting that

$$Q_{max} \equiv B + D^{-1}(1 - B) \geqslant 1 \quad \text{‘implies that’} \quad D \leqslant 1 \tag{3.16a,b}$$

on rearrangement of (3.16*a*). In conclusion, convergence towards steady flow upstream of the fracture is critically dependent on whether $D \leqslant 1$ or $D > 1$. The long-term flow in the former cases will be analysed in § 3.2. If $D > 1$ then the rate of leakage can never match the rate of injection ($Q_{max} < 1$) and, as exemplified by our solution with $D = 2$, an approach of the interface towards a steady state upstream of the fracture cannot occur. The long-term dynamics for $D > 1$ will be considered in § 3.3.

3.2. *Long-term flow for $D \leqslant 1$*

When $D \leqslant 1$, we calculate the long-term asymptotic steady state in the upstream region $0 < x < X_F$ as follows. The steady-state form of (3.3) implies that

$$\frac{h\left[1 - M(1 - h)\dfrac{\partial h}{\partial x}\right]}{h + M(1 - h)} = 1 \quad \text{and hence} \quad h = [D^2 + 2(X_F - x)]^{1/2} \tag{3.17a,b}$$

on rearrangement for $\partial h/\partial x$ and integration subject to (3.15*b*). The convergence towards the steady-state profile of (3.17*b*) is confirmed in figure 2(*a*), where (3.17*b*)

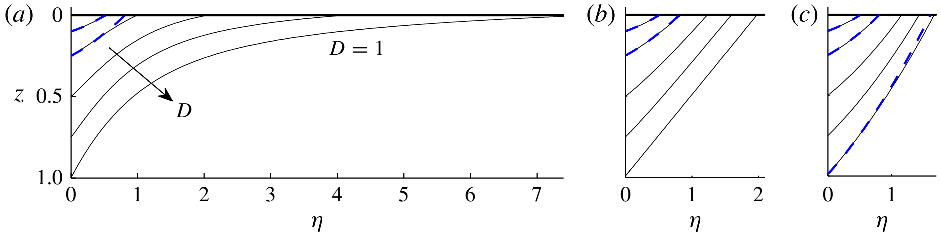

FIGURE 6. (Colour online) The numerically determined solutions of the similarity equations (3.20)–(3.22) (all solid) describing the long-term evolution of the interface h in the region $x > X_F$ when $D \leqslant 1$, shown for $D = 0.1$, 0.25, 0.5, 0.75 and 1, when (*a*) $M = 0.2$, (*b*) $M = 1$ and (*c*) $M = 5$. The numerical solutions are compared with the asymptotic solution (3.23) (dashed) that applies when $D \ll M$.

is plotted as a dotted curve. By setting $h = 1$ in (3.17*b*), we obtain the steady-state position of the lower contact line $X_U \sim X_F - (1 - D^2)/2$ shown by the line of crosses in figure 3(*a*).

By combining (3.15*a*,*b*) and (3.8*a*,*b*), we obtain the asymptotic conditions

$$h_+ = D, \quad -h_+ \frac{\partial h_+}{\partial x} = q_+ \quad \text{at } x = X_F. \tag{3.18a,b}$$

Inspection of (3.3), (3.8*b*), (3.7*a*,*b*) and (3.18*a*,*b*) reveals that there is no horizontal length scale associated with the flow described by these equations. This indicates that the asymptotic evolution of the flow downstream of the fracture can be described by a similarity solution. Motivated by the scalings between terms in these equations, we formulate the similarity variables

$$\eta = t^{-1/2}(x - X_F), \quad h = h(\eta), \quad q_+ = \mathscr{Q} t^{-1/2}, \tag{3.19a–c}$$

where $\mathscr{Q} = \mathscr{Q}(M, D)$ is the unknown coefficient of flux. In terms of (3.19*a*–*c*), equations (3.3), (3.18*a*,*b*) and (3.6*a*,*b*) transform to the ordinary differential system

$$-\frac{\eta h'}{2} + \left\{ \frac{h[\mathscr{Q} - M(1-h)h']}{h + M(1-h)} \right\}' = 0, \tag{3.20}$$

$$h(0) = D, \quad h'(0) = -\mathscr{Q}/D, \tag{3.21a,b}$$

$$h(\eta_U) = 0, \quad h'(\eta_U) = \mathscr{Q}/M - \eta_U/2, \tag{3.22a,b}$$

where a prime denotes $\mathrm{d}/\mathrm{d}\eta$. We solve (3.20)–(3.22) using a fourth-order Runge–Kutta scheme in which $\mathscr{Q}$ is treated as a shooting parameter.

A suite of solutions for $M = 0.2$, 1 and 5 are shown in figure 6(*a*–*c*), each for a selection of $D = 0.1$, 0.25, 0.5, 0.75 and 1. The shapes of the solutions are qualitatively similar to those of the similarity solutions obtained in the context of a constant-flux injection into a medium with no fracture (Pegler *et al.* 2014). Likewise, these have a long concave shape that terminates at a relatively sharp front if $M < 1$ and an approximately linear shape if $M > 1$. The specific case $M = D = 1$, shown in figure 6(*b*), is described exactly by the linear solution $h = (\eta_U - \eta)/2$ with extent $\eta_U = 2$ and coefficient of flux $\mathscr{Q} = 1$, which we used to validate our numerical solver.

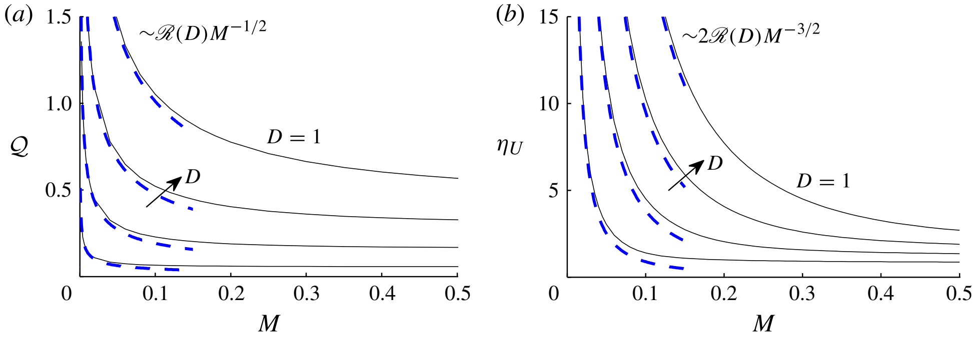

FIGURE 7. (Colour online) (*a*) The prefactor $\mathscr{Q}(M, D)$ to the long-term flux of storage $q_+ \sim \mathscr{Q}t^{-1/2}$, defined by (3.19*c*), and (*b*) the frontal similarity coordinate $\eta_U(M, D)$ plotted against the mobility ratio M for dimensionless hydrostatic parameters $D = 0.25,\ 0.5,\ 0.75$ and 1. The asymptotes (3.30*a*,*b*) that describe $\mathscr{Q}$ and η_U in the limit $M \to 0$ are shown as dashed curves.

As indicated in figure 7(*a*,*b*), both the coefficient of flux $\mathscr{Q}$ and the frontal position η_U decrease with M and tend to infinity as $M \to 0$. Analytical descriptions of these singular asymptotes, which correspond to situations relevant to CCS, will be developed later in this section.

If the dimensionless thickness of the current at the fracture is much less than the mobility ratio ($D \ll M$), then the flow is effectively unconfined (see Pegler *et al.* 2014). Equations (3.20)–(3.22) then simplify to those considered by Neufeld *et al.* (2009). By appropriately rescaling h and η_U by D, we obtain the scaled form of their universal solution to the unconfined equations as

$$h \sim Df(D^{-1/2}\eta), \quad \eta_U \sim 1.62\, D^{1/2}, \quad \mathscr{Q} \sim 0.44\, D^{3/2}, \qquad (3.23a–c)$$

for $D \ll M$, where f is a numerically determined function describing the shape of the current. The profile of (3.23*a*) is compared against our numerical solutions in figure 6, where it is plotted as a dashed curve for $D = 0.1$ and 0.25. The approximation of an unconfined aquifer is better for larger M, which is consistent with $D \ll M$ being more strongly satisfied in those cases. When $M \ll 1$, corresponding to a relatively small ambient viscosity, $D \ll M$ is satisfied for all values $D \leqslant 1$ relevant to the asymptotic regime considered here and (3.23) provides an excellent approximation in these cases (see the comparison when $D = 1$ and $M = 5$ in figure 6*c*). Note that, although (3.23) describes the long-term flow in the unconfined limit, this does not imply that confinement plays no role in leakage if $D \ll M$. Specifically, while the gradient in background pressure then has a negligible effect on horizontal flow, the leakage due to background pressure, controlled by B, can still contribute significantly in (3.4).

As noted above, both $\mathscr{Q}$ and η_U are singular as $M \to 0$. In analysing this limit, we begin by supposing that the gradient $h' = O(1)$ remains regular as $M \to 0$. Under this assumption, the second terms in both the numerator of (3.20) and in (3.22*b*), which represent gravitational spreading, are each $O(M)$ and negligible compared to the other terms. With these contributions neglected, (3.20) and (3.22*b*) simplify to

$$\left[-\frac{\eta}{2} + \frac{M}{[h + M(1-h)]^2}\right] h' = 0, \quad h'(\eta_U) = -\frac{\mathscr{Q}}{M}. \qquad (3.24a,b)$$

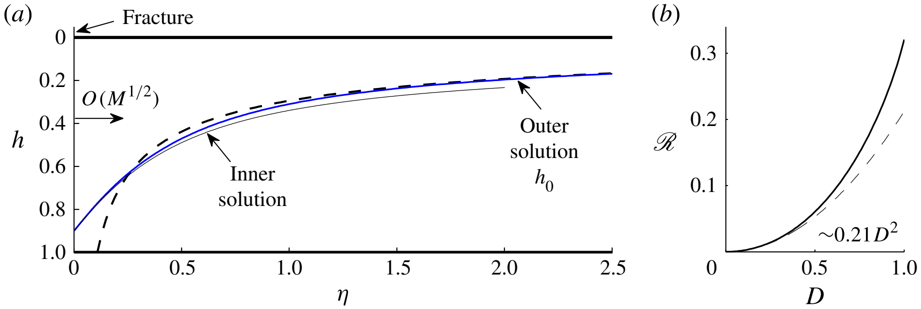

FIGURE 8. (Colour online) (*a*) The profile of the interface $h(\eta)$ of the similarity solution to (3.20)–(3.22) for the small mobility ratio $M = 0.05$ and $D = 0.9$ (grey; blue online). The inner solution governed by (3.28) and (3.29) (black, solid) and the outer solution (3.25) (black, dashed) together comprise the boundary-layer structure that emerges in the asymptotic limit $M \to 0$. (*b*) The prefactor $\mathscr{R}(D)$ to the coefficient of flux (3.30*a*) determined as part of the solution to the inner equations (3.28) and (3.29), and on which the outer solution (3.25) depends, as a function of D. The asymptotic approximation (A 3) that describes $\mathscr{R}$ in the limit $D \to 0$ is shown as a dashed curve.

Since $h' > 0$, the factor multiplying h' in (3.24*a*) must be identically zero and hence

$$h = h_0(\eta) \equiv \frac{-M + (2\mathscr{Q}M/\eta)^{1/2}}{1-M} \tag{3.25}$$

on rearrangement. The flow described by (3.25) is driven purely by the injection pressure. The profile is qualitatively similar to the injection-driven asymptotic solution describing late-time flow due to a constant-flux injection (see Pegler *et al.* (2014) and (3.32*a*) below). Like that case, (3.25) is more concave for smaller M, and the slope near the fracture is $O(M^{-3})$ larger than that downstream. Combining (3.24*b*) and (3.25), we obtain

$$\eta_U \sim 2\mathscr{Q}/M, \tag{3.26}$$

stating that η_U is proportional to the flux coefficient $\mathscr{Q}$ in the limit $M \to 0$. This is consistent with a larger retained flux producing a longer current. The inverse dependence of η_U on M reflects the tendency for background pressure to drive the current faster when it is less viscous relative to the ambient (Pegler *et al.* 2014).

The interface described by (3.25) intersects the lower boundary ($h_0 = 1$) at the positive coordinate $\eta = 2\mathscr{Q}M > 0$. Therefore, h_0 cannot provide a uniformly valid approximation to h, as indicated by the mismatch between them in figure 8(*a*). Furthermore, the conditions at the fracture (3.20*a*,*b*) cannot be imposed on h_0. This reflects the fact that, in obtaining (3.25), we neglected the highest-order derivative in (3.20). By finding when (3.25) predicts the balance of the two terms in the numerator of (3.20), we identify a boundary-layer structure in which (3.25) applies in the outer region $\eta \gg M^{1/2}$ and a different leading-order solution applies in the inner region $\eta \ll M^{1/2}$. Note that the important coefficient $\mathscr{Q}$ on which the outer solution (3.25) depends is still unknown, indicating that its determination depends on gravitational forces in the inner region neglected in obtaining (3.25).

In order to obtain the leading-order equations describing the inner solution, we recast (3.20)–(3.22) in terms of the inner variables

$$\zeta \equiv M^{-1/2}\eta, \quad \mathscr{R} \equiv M^{1/2}\mathscr{Q}, \tag{3.27a,b}$$

where ζ and $\mathscr{R}$ are of order unity in the boundary layer ($\eta \ll M^{1/2}$). The form of (3.27*b*) is motivated by a scaling between the two terms in the numerator of (3.20). On recasting (3.20) and (3.21) in terms of (3.27*a*,*b*) and neglecting higher-order terms, we obtain the simplified equations describing the flow in the inner region given by

$$-\tfrac{1}{2}\zeta h' + \mathscr{R}h^{-2} + [(1-h)h']' = 0, \quad h(0) = D, \quad h'(0) = -\mathscr{R}/D. \tag{3.28a–c}$$

The inner and outer solutions overlap in the intermediate region $M^{1/2} \ll \eta \ll 1$. Therefore, we can close (3.28*a*–*c*) by imposing the matching condition

$$h \sim (2\mathscr{R}/\zeta)^{1/2} \quad \text{as } \zeta \to \infty, \tag{3.29}$$

obtained by recasting the outer solution (3.25) in terms of ζ and neglecting the higher-order terms in the limit $\zeta \to 0$ (van Dyke's rule; see Bender & Orszag 1999). We solve (3.28) and (3.29) numerically using an adapted form of the scheme used earlier to solve (3.20)–(3.22). For the illustrative case $M = 0.05$ and $D = 5$, the inner solution (thin, black) is seen to approximate our full solution to (3.20)–(3.22) (blue) close to the fracture ($\eta \lesssim 0.5$) in figure 6(*a*). Downstream ($\eta \gtrsim 2$), the inner solution departs from the full solution, which instead approaches the outer solution (3.25) (dashed). Having determined the function $\mathscr{R}(D)$ by solving (3.28) and (3.29) over a range of D, we obtain

$$\mathscr{Q} \sim \mathscr{R}(D)M^{-1/2} \quad \text{and} \quad \eta_U \sim 2\mathscr{R}(D)M^{-3/2}, \tag{3.30a,b}$$

where (3.30*a*) follows from (3.27*b*), and (3.30*b*) follows from the combination of (3.26) and (3.30*a*). As illustrated by the dashed curves in figure 7(*a*,*b*), these asymptotes approximate our numerically determined values of $\mathscr{Q}$ and η_U in the limit $M \to 0$. The increase of $\mathscr{R}(D)$ with D illustrated in figure 8(*b*) is consistent with the dependence of $\mathscr{Q}$ and η_U on D shown earlier in figure 7(*a*,*b*). Analysis of the asymptotic limit of a small hydrostatic parameter, $D \to 0$, yields the asymptotic approximation $\mathscr{R} \sim 0.21\,D^2$ (see the appendix), shown by the dashed curve in figure 8(*b*). Combining this asymptote for $\mathscr{R}$ with (3.30*a*,*b*), $\mathscr{Q}$ and η_U are found to increase quadratically with D. In summary, storage is more efficient when D is larger and when the ambient fluid is more viscous relative to the current.

3.3. *Long-term flow for* $D > 1$

When $D > 1$ the steady-state thickness at the fracture (3.15*b*) cannot fit within the lower layer, so (3.15) cannot apply. Instead, the current fills the depth of the lower layer ($h(X_F, t) = 1$) and the lower contact line overshoots the fracture ($X_L > X_F$). Once that occurs, leakage is fixed at the maximum rate Q_{max} in (3.12). Therefore,

$$q_F = Q_{max} \equiv B + D^{-1}(1-B) \quad \text{and} \quad E = q_+ = 1 - Q_{max}. \tag{3.31a,b}$$

The approach towards the long-term constant efficiency (3.31*b*) is illustrated by the examples with $D > 1$ shown in figure 5(*b*).

Once the storage efficiency q_+ becomes fixed at the constant value (3.31*b*), the conditions on flow in front of the fracture ($x > X_F$) become equivalent to those associated with a source of constant strength $q_+ \equiv 1 - Q_{max}$, as analysed by Pegler *et al.* (2014). Given the asymptotic solutions described in that study, we can identify the long-term asymptotic interface and contact lines downstream of the fracture as

$$h \sim \frac{-M + (q_+ M t/x)^{1/2}}{1-M}, \quad X_U \sim M^{-1} q_+ t, \quad X_L \sim M q_+ t. \tag{3.32a–c}$$

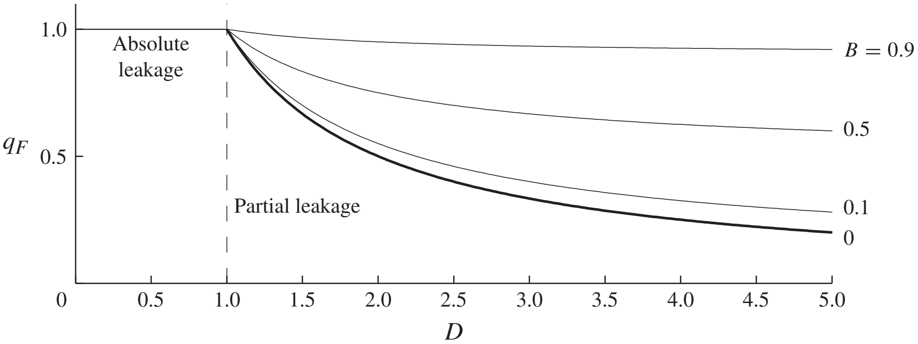

FIGURE 9. The long-term asymptotic rate of leakage q_F as a function of the dimensionless parameter D for a selection of $B = 0.01$, 0.1, 0.5 and 0.9. The plot illustrates how q_F is unitary for all values of $D \leqslant 1$ in accord with (2.21*a*), for which effectively all the injected fluid leaks through the fracture at large times, and decays with D for $D > 1$ in accord with (2.21*b*), for which only a fraction of the fluid injected into the medium leaks through the fracture. The special case $B = 0$ for which $q_F \sim D^{-1}$, corresponding to purely hydrostatic leakage, is shown by the thick curve.

This applies when $M \leqslant 1$ (see Pegler *et al.* (2014) for the different late-time regime that applies when $M > 1$). The asymptotic height (3.32*a*) is plotted as a dashed curve in figure 2(*b*) for $D = 2$, where it is seen to approximate the numerical solution. The long-term positions of the contact lines (3.32*b*,*c*) show good agreement with our numerical solution in figure 3(*b*). In the joint limit $B \to 0$ and $D \to \infty$, there is no leakage ($q_+ \to 1$) and the asymptote (3.32) recovers that which applies when there is no leakage.

In summary, the long-term rates of leakage given by (3.15*a*) or (3.31) are

$$q_F \sim \begin{cases} 1 & \text{if } D \leqslant 1, \\ B + D^{-1}(1 - B) < 1 & \text{if } D > 1. \end{cases} \tag{3.33a,b}$$

In general then, the asymptotic value of q_F depends only on B and D. The plot of q_F in figure 9 illustrates that, when $D \leqslant 1$, absolute leakage occurs ($q_F \to 1$), independent of B. When $D > 1$, q_F tends to the value (3.33*b*), which is less than unity, and only a fraction of the fluid injected ultimately leaks. The value of q_F increases with B because these cases imply greater background leakage. Purely hydrostatic leakage ($B = 0$) (thick curve) provides the minimum leakage rate for a given hydrostatic parameter D.

3.4. *Transient leakage*

While the long-term rate of leakage (3.33*a*,*b*) depends on B and D alone, the transient evolution of the leakage rate of injected fluid $q_F(t)$ towards its asymptotic value is dependent on all the parameters M, B, D and X_F. To indicate the influence of B, we have plotted $q_F(t)$ in figure 10(*a*) for a selection of $B = 0.1$, 0.5 and 0.9, with $M = 0.2$, $D = 2$ and $X_F = 2$ all held fixed. The main effect of B is to alter the time when the flux of the current towards the fracture first exceeds the minimum rate of leakage ($q_- = B$), indicated by a dot for each solution. Before this time, the evolution follows the same curve given by the special solution in which all fluid flowing towards the fracture

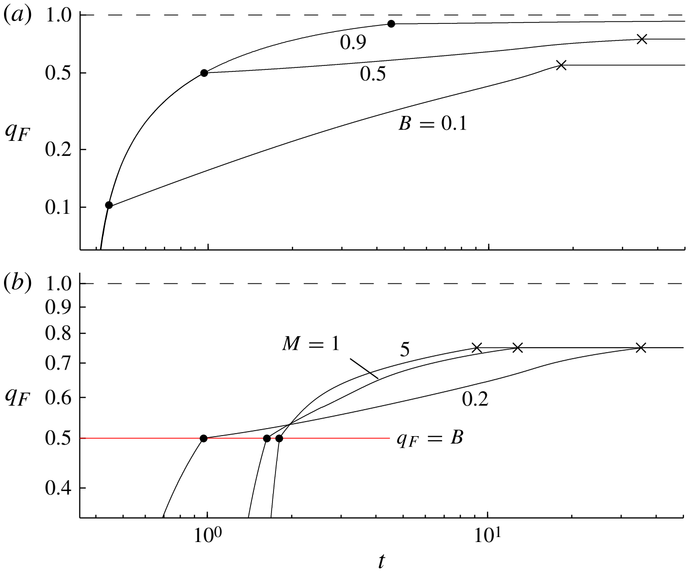

FIGURE 10. (Colour online) The evolution of the dimensionless rate of leakage q_F for (*a*) a selection of $B = 0.1$, 0.5 and 0.9 with $D = 2$, $M = 0.2$ and $X_F = 2$ held fixed, and (*b*) a selection of $M = 0.2$, 1 and 5 with $B = 0.5$, $D = 2$ and $X_F = 2$ held fixed. In (*b*), the minimum rate of leakage $q_F = B$ at which the current begins to propagate into the region $x > X_F$ is shown by a horizontal grey (red online) line. In both panels, the dimensionless flux of injection $q = 1$ is shown by a horizontal dashed line.

leaks through it unconditionally ($B = 1$). While $q_F < B$, the flow is independent of both leakage parameters (B and D). Only once $q_- > B$, and leakage becomes controlled dynamically by the leakage law (2.18), do the solutions with different B begin to realize different asymptotic rates of leakage in accord with (3.33*b*). The time when this occurs is smaller when B is larger because in those cases the current propagates downstream of the fracture earlier and its vertical accumulation below the fracture is more delayed.

To indicate the effect of the mobility ratio M on the transient flow, we have plotted the variation of the evolution $q_F(t)$ with $B = 0.5$ and $D = 2$ held fixed for a selection of $M = 0.2$, 1 and 5 in figure 10(*b*). As implied by (3.33*a*,*b*), the leading-order long-term leakage is independent of M, so all the solutions shown in figure 10(*b*) have the same late-time value. Since increasing M implies a slower current (Pegler *et al.* 2014), larger values of M delay the initiation of leakage. However, the flux of leakage for $M > 0.2$ soon overtakes the example with $M = 0.2$ because those cases result in a longer and thinner current that takes more time to accumulate below the fracture.

4. Geophysical discussion

We form illustrative estimates of the four parameters given by (3.11*a*–*d*) motivated by the ongoing CCS operation at the Sleipner field (Bickle *et al.* 2007). The formation at Sleipner is divided into a number of stacked, roughly horizontal sandstone layers of typical thicknesses (H or H_2) varying between 5 and 20 m, separated by interstitial layers of mudstone of typical thicknesses between 1 and 5 m (Boait *et al.* 2012). Seismic data have shown that the injected CO_2 has migrated vertically through a series of porous layers. The interstitial layers therefore contain fractures or localized regions of leakage.

The ratios between the depths of any two stacked layers can be characterized as $\Gamma \equiv H/H_2 \approx 0.25$–4, for which the leakage parameter (3.11*b*) lies in the broad range $B \approx 0.2$–0.8. The dynamic viscosity of CO_2 and ambient water can be characterized by $\mu \approx 10^{-4}$ Pa s and $\mu_a \approx 10^{-3}$ Pa s, respectively, and hence their ratio $M \approx 0.1$. The density difference is roughly $\Delta\rho \approx 300$ kg m^{-3}. The volumetric rate of injection is $2\mathscr{W} Q_0 \approx 0.04$ m^3 s^{-1} (equivalent to 1 Mt yr^{-1}), where we have set $\mathscr{W} \approx 1$ km as the characteristic extent of the CO_2 current (Boait *et al.* 2012), giving the flux per unit width $Q_0 \approx 5 \times 10^{-5}$ m^2 s^{-1}. With these estimates, the intrinsic length and time scales (3.2*a*,*b*) are $\mathscr{L} \approx 1$ km and $\mathscr{T} \approx 6$ years. The hydrostatic parameter (3.11*c*) is then found to be $D = O(10)$. Background pressure, which was neglected in previous studies considering unconfined media, is thus indicated to be significant in driving leakage through the formation ($Q_G = O(10^{-1} Q_B)$). This is because the pressure introduced by the injection is much greater than the maximum possible gravitational pressure head. For less permeable aquifers, like that at In Salah (Vasco, Ferretti & Novali 2008), D would be yet larger.

Using the parameter estimates given above, we perform an illustrative calculation of our model predictions. We assume that the depth of the sandstone layer into which fluid is injected is comparable to that into which the current leaks, so $H = H_2$ and $B = 0.5$. We also set $M = 0.1$ and $D = 10$. The long-term asymptotic rate of leakage is then predicted by (3.33*b*) to be $q_F \sim 0.55 Q_0$. Note that 90 % of this contribution to leakage is driven by the background pressure. The remaining 10 % is due to the gravitational hydrostatic head.

We use an illustrative fracture position $x_F = 2$ km, for which the dimensionless form (3.11*d*) is given by $X_F \equiv x_F/\mathscr{L} = 2$. In figure 11(*a*,*b*), we have plotted the evolution of the depth of the current below the fracture normalized by the depth of the aquifer, h/H, and the rate of leakage of the current normalized by its rate of injection, q_F/Q_0. The time taken for the current to reach the fracture is just $t \approx 1.2$ years. The front of the current then remains pinned at the fracture for a duration of three years before overshooting it. When that occurs, the leakage rate is already within 90 % of its long-term value. The duration of approximately four years on which this 90 % level is reached is much shorter than the current 18-year running time of the Sleipner project. The subsequent enhancement of leakage due to the development of the hydrostatic head below the fracture adds the remaining 10 % contribution to the leakage rate over the much longer period of approximately 200 years. This is consistent with the currents in the sandstone layers at Sleipner not yet having spanned the depth of any layer (Boait *et al.* 2012). The relatively insignificant addition to leakage due to accumulation of the current below the fracture contrasts sharply with the predictions of unconfined models, where most leakage stems from this accumulation. Boait *et al.* (2012) note that, while vertical migration through a series of interstitial layers is evident at Sleipner, the planforms of the CO_2 currents in the sandstone horizons between them do not show much evidence of slowing down in response to their growth. The relatively rapid onset of steady leakage predicted by our model could explain how the leakage rates can remain largely constant despite the continued accumulation of currents through the interstitial layers.

The calculation above provides an insightful illustration of the first-order effects of confinement on leakage in a geological formation. Note, however, that real aquifers contain three-dimensional variations in topography, as well as anisotropic and heterogeneous permeabilities, not accounted for by our idealized model.

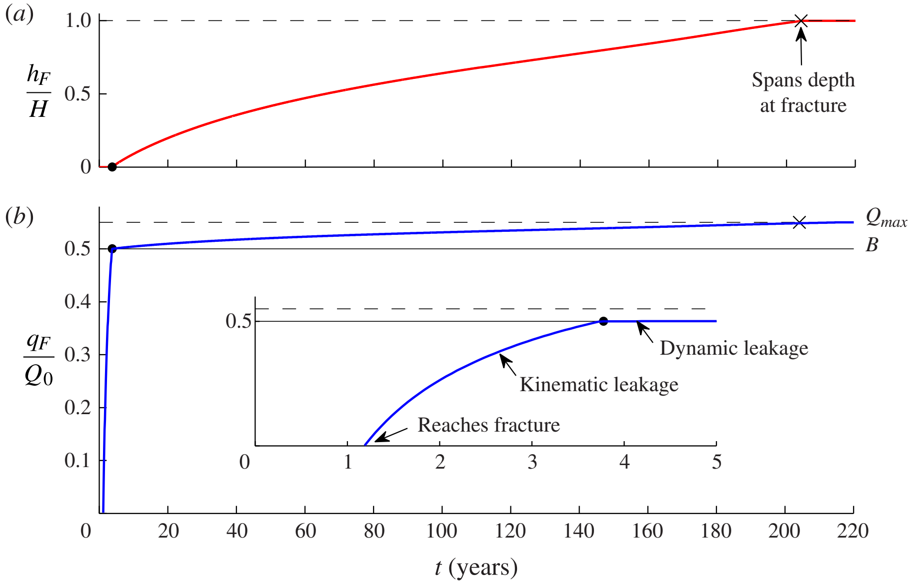

FIGURE 11. (Colour online) The evolution of (*a*) the thickness of the current below the fracture normalized by the thickness of the aquifer, h_F/H, and (*b*) the rate of leakage of injected fluid normalized by its rate of injection, q_F/Q_0, for parameter settings motivated by the geophysical example in § 4. In (*a*), the thickness of the aquifer $h=H$ is shown as a horizontal dashed line. In (*b*), the leakage due to background pressure B is shown as a horizontal solid line and the maximum rate of leakage Q_{max} is shown as a horizontal dashed line. In both panels, the time at which leakage switches from kinematic to dynamic leakage is indicated by a filled circle. The time at which the current first spans the depth of the aquifer below the fracture is indicated by a cross.

Three-dimensional spreading from a point injection, for example, may introduce long-term asymptotic regimes different from those that we have identified. The effect of a spatially dependent background pressure (2.13) may also allow leakage due to the hydrostatic head to have a greater impact on leakage relative to the background pressure to further distances from the injection. Other physics excluded from our model include the compressibility of the injected and ambient fluids. With compressible ambient fluid, for example, pressure diffuses with diffusivity $\mathscr{D} \equiv \lambda_a K$, where $K \approx 3 \times 10^8$ is the bulk modulus of water (Dake 2010). Pressure disturbances therefore propagate for distances of $x \sim 2\sqrt{\mathscr{D}t} \approx 10$ km in one year and 30 km in 10 years. When flow is incompressible ($\mathscr{D} = \infty$), as we have assumed, pressure disturbances instead propagate infinitely fast and dynamics respond instantaneously to far-field conditions like (2.1). This may provide a good approximation over long time scales of several decades or more, when the communication between the current and the far field becomes faster relative to the time scales of the flow. However, on time scales of a year or less, the pressure disturbance due to the injection has yet to interact with the downstream condition (2.1) if $L = O(10 \text{ km})$, indicating that compressible dynamics may play an important role at early times.

5. Conclusions

We have shown that the confinement of flow in a porous geological formation by a lower boundary leads to fundamentally new dynamical controls on the leakage of buoyant injected fluid. Generally, it has two distinct effects.

First, confinement introduces a background pressure associated with driving fluid horizontally along the length of the aquifer. The build-up of back-pressure due to the flow of ambient fluid along the lengths of the lower and upper aquifers – the former promoting leakage and the latter resisting it – sets a background rate of leakage independent of gravitational effects. Generally, this enhances leakage at early times. The resistance to leakage due to displacing ambient fluid along the upper layer can be orders of magnitude larger than that due to the viscous stresses acting in the interior of the fracture itself.

Second, confinement constrains the maximum possible leakage by limiting the gravitational hydrostatic head of buoyant fluid below the fracture. The resulting maximum rate of total leakage Q_{max} has significant implications for the long-term storage efficiency, or proportion of injected fluid retained. More specifically, two possible long-term flow regimes emerge dependent on whether the dimensionless parameter $D \equiv lQ_0/bHU$ satisfies $D \leqslant 1$ or $D > 1$.

When $D \leqslant 1$, the interface of the current approaches a height $h \sim DH$ below the fracture. Upstream of the fracture, the current becomes steady. Downstream, it converges towards a similarity solution that extends in proportion to $t^{1/2}$. The long-term storage efficiency decays as $E \sim \mathscr{Q} t^{-1/2}$, where $\mathscr{Q}$ is the constant coefficient of storage, implying that most fluid injected leaks at long times. If the injected fluid is much less viscous than the ambient ($M \rightarrow 0$), as is relevant to CCS, then an asymptotic structure emerges downstream of the fracture comprising an inner region of extent $O([Mt]^{1/2})$, wherein both gravity and background pressure control the flow, connected to an outer region dominated by background pressure. The dynamics in the inner region independently determine the coefficient of storage $\mathscr{Q}$. Analysis of the inner equations showed that $E \approx 0.21\, D^2 (Mt)^{-1/2}$, implying more efficient storage with less viscous injected fluid.

When $D > 1$, the thickness of the injected fluid layer accumulates to fill the entire depth of the medium below the fracture. Unlike when $D \leqslant 1$, the long-term efficiency of storage does not decay to zero and instead approaches the positive value $E \rightarrow 1 - Q_{max}$. Hence, while confinement causes greater leakage at earlier times by the introduction of background pressure, the constraint on the maximum hydrostatic head below the fracture has the potential to mitigate leakage by orders of magnitude if $D > 1$.

Analysis of the model predictions in the context of Sleipner reveals that background pressure may be dominant in driving leakage between the interstitial layers. The results indicate that the accumulation of the hydrostatic head below the fractures, assumed dominant in studies of unconfined aquifers, plays a relatively minor role. The propensity for thinner reservoirs to better constrain the hydrostatic head and provide more secure storage presents a potentially vital consideration in the assessment of long-term CO_2 storage in underground aquifers.

Acknowledgements

This work was supported by the PANACEA project funded by the European Commission. The research of J.A.N. is supported by a Royal Society University Research Fellowship. H.E.H. is partially supported by a Wolfson Royal Society merit award.

Appendix A. The asymptotic solution for small D

We develop the asymptotic solution to the inner equations (3.28) and (3.29) that applies in the limit of a small hydrostatic head $D \rightarrow 0$. To do this, we recast these equations in terms of the scaled variables

$$h \equiv DF(\zeta) \quad \text{and} \quad \mathscr{R} \equiv D^2 \mathscr{S}, \tag{A 1a,b}$$

where $F(\zeta)$ and $\mathscr{S}$ are assumed to be of order unity. On applying the approximation $h \sim D \ll 1$, (3.28) and (3.29) reduce to

$$-\tfrac{1}{2}\zeta F' + \mathscr{S} F^{-2} + F'' = 0, \quad F(0) = 1, \quad F'(0) = -\mathscr{S}, \quad F(\infty) \sim \zeta^{-1/2}, \tag{A 2a–d}$$

respectively, where we have used a prime here to denote $\mathrm{d}/\mathrm{d}\zeta$. There are no free parameters in this reduced set of equations, implying that their solution represents a special curve that uniquely describes the asymptotic solution to (3.28) and (3.29) in the limit $D \to 0$. By solving (A 2*a–d*) using an adapted form of our numerical scheme used earlier to solve (3.20)–(3.22), we obtain the prefactor $\mathscr{S} \approx 0.21$. Combination of this value of $\mathscr{S}$ with (A 1*b*) determines the asymptotic relationship for the scaled coefficient of storage,

$$\mathscr{R} \sim 0.21 D^2 \quad \text{as } D \to 0, \tag{A 3}$$

which we have plotted as a dashed curve in figure 8(*b*).

REFERENCES

Bear, J. 1988 *Dynamics of Fluids in Porous Media*. Dover.

Bender, C. M. & Orszag, S. A. 1999 *Advanced Mathematical Methods for Scientists and Engineers, vol. I: Asymptotic Methods and Perturbation Theory*. Springer.

Bickle, M. J. 2009 Geological carbon storage. *Nat. Geosci.* **2**, 815–818.

Bickle, M. J., Chadwick, R. A., Huppert, H. E., Hallworth, M. A. & Lyle, S. 2007 Modelling carbon dioxide accumulation at Sleipner: implications for underground carbon storage. *Earth Planet. Sci. Lett.* **255**, 164–176.

Boait, F. C., White, N. J., Bickle, M. J., Chadwick, R. A., Neufeld, J. A. & Huppert, H. E. 2012 Spatial and temporal evolution of injected CO_2 at the Sleipner Field, North Sea. *J. Geophys. Res.* **117**, B03309.

Dake, L. P. 2010 *Fundamentals of Reservoir Engineering*. Elsevier.

Huppert, H. E. & Neufeld, J. A. 2014 The fluid mechanics of carbon dioxide sequestration. *Annu. Rev. Fluid Mech.* **46**, 255–272.

Huppert, H. E. & Woods, A. W. 1995 Gravity-driven flows in porous layers. *J. Fluid Mech.* **292**, 55–69.

Neufeld, J. A., Vella, D. & Huppert, H. E. 2009 The effect of a fissure on storage in a porous medium. *J. Fluid Mech.* **639**, 239–259.

Neufeld, J. A., Vella, D., Huppert, H. E. & Lister, J. R. 2011 Leakage from gravity currents in a porous medium. Part I. A localized sink. *J. Fluid Mech.* **666**, 391–413.

Nordbotten, J. M. & Celia, M. A. 2006 Similarity solutions for fluid injection into confined aquifers. *J. Fluid Mech.* **561**, 307–327.

Nordbotten, J. M., Celia, M. A., Bachu, S. & Dahle, H. 2005 Semianalytical solution for CO_2 leakage through an abandoned well. *Environ. Sci. Technol.* **39**, 602–611.

Nordbotten, J. M., Kavetski, D., Celia, M. A. & Bachu, S. 2009 Model for CO_2 leakage including multiple geological layers and multiple leaky wells. *Environ. Sci. Technol.* **43**, 743–749.

Orr, F. M. 2009 Onshore geological storage of CO_2. *Science* **325**, 1656–1658.

Pegler, S. S., Huppert, H. E. & Neufeld, J. A. 2014 Fluid injection into a confined porous layer. *J. Fluid Mech.* **745**, 592–620.

Pritchard, D. 2007 Gravity currents over fractured substrates in a porous medium. *J. Fluid Mech.* **584**, 415–431.

PRITCHARD, D. & HOGG, A. J. 2001 On the slow draining of a gravity current moving through a layered permeable medium. *J. Fluid Mech.* **444**, 23–47.

SINGHAL, B. B. S. & GUPTA, R. P. 2010 *Applied Hydrogeology of Fractured Rocks*. Springer.

VASCO, D. W., FERRETTI, A. & NOVALI, F. 2008 Reservoir monitoring and characterization using satellite geodetic data: interferometric synthetic radar observations from the Krechba Field, Algeria. *Geophysics* **73**, WA113–122.

VELLA, D., NEUFELD, J. A., HUPPERT, H. E. & LISTER, J. R. 2011 Leakage from gravity currents in a porous medium. Part II. A line sink. *J. Fluid Mech.* **666**, 414–427.